

NASA Contractor Report 187467

ICASE Report 90--77

AD-A229 670

# ICASE

## FLOW ESTABLISHMENT IN A GENERIC SCRAMJET COMBUSTOR

P. A. Jacobs  
R. C. Rogers  
E. H. Weidner  
R. D. Bittner

Contract No. NAS1-18605  
October 1990

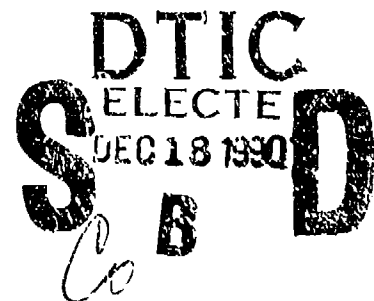
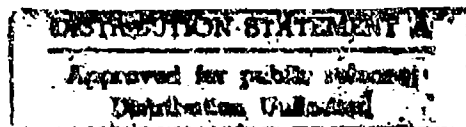
Institute for Computer Applications in Science and Engineering  
NASA Langley Research Center  
Hampton, Virginia 23665-5225

Operated by the Universities Space Research Association



National Aeronautics and  
Space Administration

Langley Research Center  
Hampton, Virginia 23665-5225



# FLOW ESTABLISHMENT IN A GENERIC SCRAMJET COMBUSTOR

P. A. Jacobs<sup>1</sup>

Institute for Computer Applications in Science and Engineering  
NASA Langley Research Center  
Hampton, VA 23665

R. C. Rogers<sup>2</sup> & E. H. Weidner<sup>3</sup>

Hypersonic Propulsion Branch  
NASA Langley Research Center  
Hampton, VA 23665

R. D. Bittner<sup>4</sup>

Analytical Services and Materials, Inc.  
Hampton, VA 23666

## ABSTRACT

The establishment of a quasi-steady flow in a generic scramjet combustor is studied for the case of a time varying inflow to the combustor. Such transient flow is characteristic of the reflected-shock tunnel and expansion-tube test facilities. Several numerical simulations of hypervelocity flow through a straight-duct combustor with either a side-wall-step fuel injector or a centrally-located strut injector are presented. Comparisons are made between impulsively started but otherwise constant flow conditions (typical of the expansion-tube or tailored operation of the reflected-shock tunnel) and the relaxing flow produced by the "undertailored" operation of the reflected-shock tunnel. Generally the inviscid flow features, such as the shock pattern and pressure distribution, were unaffected by the time varying inlet conditions and approached steady state in approximately the times indicated by experimental correlations. However, viscous features, such as heat transfer and skin friction, were altered by the relaxing inlet flow conditions. *Keywords: Supersonic combustion; Turbine engines; Shock tunnels; Mathematical models; --*

<sup>1</sup>Research was supported by the National Aeronautics and Space Administration under NASA Contract No. NAS1-18605 while the author was in residence at the Institute for Computer Applications in Science and Engineering (ICASE), NASA Langley Research Center, Hampton, VA 23665-5225.

<sup>2</sup>Senior Research Scientist, Member AIAA.

<sup>3</sup>Research Scientist.

<sup>4</sup>Research Scientist, Hypersonic Technology Office.

*Also see: Air & Space; Jet engine inlets; heat transfer; Fluid mechanics; Turbine engines; Hypersonic flow; Turbine engines; Inlets; Shock tunnels; Mathematical models; Hypersonic velocity; Aerodynamics; --*

## 1. INTRODUCTION

The National Aero-Space Plane (NASP) project has been the focus of the recent revival of hypersonic aerodynamics and propulsion research. Propulsion studies for the high Mach number range ( $M_{flight} > 4$ ) have concentrated on the air-breathing supersonic-combustion ramjet (scramjet) using hydrogen as the primary fuel. Most of the early research studies of the mixing and combustion processes in a scramjet relied on conventional ground test facilities in which the test gas is heated to flight enthalpy by combustion of hydrogen or with an electric arc. These tests have generally been limited to  $M_{flight} < 8$  because of the limited total temperatures available with these facilities. Generation of test flows with enthalpies relevant to the flight regime,  $10 < M_{flight} < 25$ , requires a different approach.

One type of facility capable of this high enthalpy range is the pulse-type facility in which the test gas is rapidly heated by the passage of a strong shock wave. Two examples of pulse facilities are the reflected-shock tunnel and the expansion tube. A review of these facilities and their use in experimental hypervelocity aerodynamics has been presented by Stalker [1]. When using pulse facilities to simulate high enthalpy flows, a number of trade-offs between test time and test gas conditions must be made. One of the difficulties in using pulse facilities to test supersonic combustors is that the test times are relatively short - on the order of one-half millisecond. These short test times are a concern because, even in steady flow, many of the important flow processes in the combustor will take significant time to become established (i.e., approach steady state). With a transient flow the establishment may be further delayed.

Much effort has been directed toward the optimization of the scramjet combustor and, in particular, to the efficiency of fuel-air mixing and reaction so as to obtain minimum length and wall heat load in the engine. Because of the high velocity, high temperature and low density of the combustor flow, the mixing of the fuel and air is relatively slow at the higher flight speeds. Consequently, mixing augmentation and enhancement by the controlled generation of turbulence and/or large-scale vortices in the mixing and flame-holding zones are being examined in both numerical studies [2] and experimental studies [3]. These techniques generally involve some type of recirculating flow in the wake of a body, step or transverse jet and hence require some finite time to reach steady state (or a quasi-periodic state).

The focus of this study is to examine several time accurate simulations of steady and transient flow through a generic scramjet in an attempt to assess the following issues:

- The time required for the flow in the wake region of the fuel injector (without injection) to become established relative to the typical test times available in pulse facilities.



- The impact of test flow relaxation (as encountered in the undertailored operation of a reflected-shock tunnel) on the approach to steady state combustor flow.
- The validity of using the "hypersonic equivalence principle" (see, e.g., [4]) to transform the relaxing flow to a quasi-steady flow.

The flow through the supersonic combustor was computed at the high enthalpy, short duration, and sometimes transient conditions typical of a shock tunnel or expansion tube. Calculations of the combustor flow were made in a time-accurate manner using the Navier-Stokes code SPARK [5], [6]. This code has been previously applied to the simulation of scramjet flows with fuel injection and a thrust ramp in a shock tunnel environment [7]. In the present study the code is used to compute the basic combustor flow without fuel injection.

## 2. OPERATION OF PULSE FACILITIES

A brief description of the operation of two particular pulse facilities will be given in this section. The first is a free-piston driven reflected-shock tunnel, T4, located at the University of Queensland [8]. The second is an expansion tube, HYPULSE, located at General Applied Science Laboratories, New York [9].

### 2.1. Reflected-Shock Tunnel

The principal features of a shock tunnel and its operation are shown in Figure 1. The driver tube, which initially contains low pressure helium, and the shock tube which contains the test gas are separated by the primary diaphragm. Attached to the downstream end of the shock tube is a nozzle whose throat is significantly smaller than the diameter of the shock tube. The test gas is contained by a thin mylar diaphragm which separates the shock tube from the evacuated test region.

The first stage of operation of the T4 facility is the launch of the piston and its acceleration down the compression tube. The driving force is supplied by the compressed air from the reservoir. The primary diaphragm, which is typically composed of two sheets of 2mm mild steel, subsequently bursts at a pressure 56.6 MPa. At this point, the helium has been compressed to 1/60th of its initial volume and is contained in approximately 0.5m of the compression tube.

After diaphragm rupture, helium driver gas expands into the shock-tube and compresses the low pressure test gas before it. The incident shock travels the length of the shock tube, reflects from the closed end of the tube and brings the test gas to rest in the nozzle

supply region. Operation in this manner is called "tailored" [10] and is shown in the (x-t) diagram (Figure 1(b)) by the contact surface coming to rest when intercepted by the reflected shock. The compressed test gas is contained in the nozzle supply region in a length of approximately 0.25 – 0.5m. Ideally, the nozzle supply conditions are maintained as the reflected shock continues upstream through the driver gas.

Upon shock reflection, the light secondary diaphragm bursts and some of the compressed test gas expands into the nozzle. Smith [11] has provided a quasi-one-dimensional model for the nozzle starting processes.

For combustion studies, the useful test time is terminated by the contamination of the test gas by the driver gas. The mechanism for this contamination is the bifurcation of the reflected shock into two weaker oblique shocks near the wall of the tube. This mechanism has been studied in [12] and has been shown to occur for undertailored conditions at high enthalpies [13]. For undertailored operation, conditions are such that, when the reflected shock reaches the helium-air interface, it accelerates into the helium and an expansion propagates into the nozzle supply gas. With no other influences, the supply region will reach a new equilibrium but there will be a significant and unavoidable drop in nozzle supply pressure  $P_s$  shortly after shock reflection. The expansion of the test gas slug delays the arrival of helium jetting down the walls of the shock tube and prolongs the useful test time. The approximate time at which contamination of the test gas is expected to reach the nozzle throat decreases with increasing stagnation enthalpy,  $H_s$ , (see, e.g., [1]).

The effect of finite driver size upon the relaxation of  $P_s$  is also noticeable. Stalker [14] has suggested a mode of operation where the motion of the piston (after rupture) maintains approximately constant conditions in the driver tube while nearly 50% of the helium flows into the shock tube. Following this initial period, of approximately 1ms, the pressure in the driver decays rapidly and this decay is transmitted downstream along a  $(u+a)$  characteristic. The effect of the finite volume of the driver tube is that the decay in  $P_s$  may start early in the test period.

The net result is that the history of the nozzle supply pressure and a representative pitot pressure at the exit plane of the Mach 5 nozzle will appear as shown in Figure 2. The pressure transducer measuring  $P_s$  is located a few centimetres upstream of the reflecting end of the shock tube. Its trace shows the passage of the incident shock and the arrival of the reflected shock. Due to transducer rise time and location, the full reflected pressure is not recorded. Past the peak value, there is a continuous decay in  $P_s$  due to the combined effects of undertailored operation and driver pressure decay. For helium driver gas and operation considered here, this decay is typically 25 – 30% during a nominal 0.5ms test time [15]. Note the delay between the supply pressure trace and the pitot pressure trace. This delay will be

used in the normalization procedure discussed in Section 3.5.

## 2.2. Expansion Tube

An expansion tube facility consisting of a driver tube (initially containing high pressure driver gas), a shock tube (containing the test gas) and an acceleration tube (containing low pressure acceleration gas) is shown schematically in Figure 3. The driver tube and shock tube are separated by the primary diaphragm and the acceleration tube is separated from the shock tube by a secondary (and very light) diaphragm. The shock- and acceleration tubes have the same diameter. Although the HYPULSE facility has a fixed driver tube rather than a free-piston driver, the gas-dynamic processes in the shock tube are similar.

The operation is initiated by the rupture of the primary diaphragm. High pressure driver gas flows into the shock tube and the incident shock compresses and accelerates the test gas. On reaching the end of the shock tube, the secondary diaphragm bursts (ideally without causing disturbance) and the shock-compressed test gas expands into the low pressure gas in the acceleration tube. The pressure to which the acceleration gas rises is below the pressure of the bulk of the shock-compressed test gas and so the downstream portion of the test gas undergoes an unsteady expansion to the test flow conditions.

The test time commences after the test-gas/acceleration-gas interface arrives and usually finishes with the arrival of the downstream end of the unsteady expansion fan. Figure 4 shows a typical history of the static pressure in the test region. The trace shows a rapid rise due to the shock through the acceleration gas, a slower rise (possibly due to diffuser starting processes) to the test conditions at approximately  $60\mu s$  and then roughly constant until the arrival of the unsteady expansion  $400\mu s$  later.

## 3. NUMERICAL SIMULATION

The computations of flow through the generic supersonic combustor were made with the Langley Research Center SPARK-2D code. This two-dimensional, elliptic, finite difference code was developed by J. P. Drummond [5], [6] to integrate the conservation equations for mass, momentum and energy in a time accurate manner. Since the primary concern is the temporal development of the combustor flow features, the scope of the modelling was reduced by considering only laminar flow of a nonreacting test gas and avoiding the fuel injection and mixing issues. The effects of transition, turbulence, mixing and chemistry will be examined in future studies.

### 3.1. Combustor Geometry and Boundary Conditions

A generic scramjet combustor, typical of those tested in the reflected shock tunnel T4 [15], is shown in Figure 5. This model consists of the major features of a scramjet combustor, including some form of injector (with an associated wake/mixing region) and a set of confining walls (with their associated boundary layers).

To perform the two-dimensional computations, the scramjet combustor duct in Figure 5 was modelled as shown in Figure 6. Only half of the duct was considered in the computational domain. Two classes of calculations were performed which differed in the location of the inflow boundary. Cases 1,2,3 and 6 with the inflow boundary at the start of the duct walls ( $x = 0$ ), have a flow domain as shown at the top of Figure 6. These are called the "short" injector cases. Cases 4 and 5, with the inflow boundary at the injector strut leading edge ( $x = -0.138m$ ), are called the "long" injector cases (Figure 6(b)). Descriptions of the six cases considered in this study are shown in Table 1.

Boundary conditions on the wall (at  $y = 0.02357m$ ) and the surfaces of the injector were set to zero velocity, zero normal pressure gradient and a fixed temperature  $T = 300K$  (i.e., cold wall). Cases 4 and 5 included a free boundary along  $y = 0.02357m$  for  $-0.138m < x < 0m$ . Conditions at the inflow plane were supersonic. The outflow boundary at  $x = 0.5m$  was specified as supersonic with zero gradients in the flow direction. In Cases 1 and 2, the x-axis downstream of the injector ( $x > 0.114$ ) was set as a cold wall so as to provide a situation close to that found in parallel wall injection studies. Cases 3,4,5 and 6 set this line to be a symmetry plane with zero normal velocity and zero normal gradients for pressure, temperature, and tangential velocity.

### 3.2. Grids

The grids used in the computation are shown in Figure 7. The entire domains, including the injectors, were included in the grids and during the computation all grid points within the injector were reset to initial conditions. Each grid consisted of a number of separate zones in which the nodes were clustered at one or more of the zonal edges so that large flow gradients near the boundaries and planes defining the injector could be resolved without excessive computational expense.

The x and y coordinates for the grids used in the short injector cases were independently generated using one of Roberts' [16] stretching transformations. (See also [17], Section 5-b.1). In each zone there were  $N + 1$  nodes, including the end points, located at

$$z = z_a \bar{\eta} + z_b(1 - \bar{\eta}), \quad (1)$$

where

$$\bar{\eta} = \frac{[(\beta + 2\alpha)\lambda - \beta + 2\alpha]}{(2\alpha + 1)[1 + \lambda]}, \quad (2)$$

$$\lambda = \left( \frac{\beta + 1}{\beta - 1} \right)^{(\eta - \alpha)/(1 - \alpha)}, \quad (3)$$

$$\eta = \frac{j}{N}, j = 0 \dots N. \quad (4)$$

Details of the zonal boundaries and stretching parameters are given in Table 2. These parameters were adjusted until numerical artifacts were eliminated from flow monitors such as the length of the recirculation region behind the injector (discussed in Section 4.3) and the position of the recompression shock (discussed in Section 4.4). Note that, for  $\alpha = 0$ , the nodes are clustered close to the  $z_a$  end of the zone and, for  $\alpha = 0.5$ , the nodes are clustered close to both boundaries.

For the long injector cases, the y-coordinates were generated in a similar manner. However, the x-coordinates were generated using a compression function due to Thomas et al. [18]. In each zone there were  $N + 1$  nodes (including end points) specified by Equation 1 and

$$\bar{\eta} = \eta_0 \left[ \frac{\sinh(\beta\eta - A_\eta)}{\sinh(A_\eta)} + 1 \right], \quad (5)$$

where

$$A_\eta = \frac{1}{2} \ln \left[ \frac{1 + (e^\beta - 1)\eta_0}{1 + (e^{-\beta} - 1)\eta_0} \right], \quad (6)$$

and  $\eta_0$  is the value of  $\eta$  at which maximum compression occurs. Details of the zonal boundaries and stretching parameters are given in Table 3.

### 3.3. Initial Conditions and Inflow Conditions

The initial conditions within the combustor were set to  $T = 300K$ ,  $P = 300Fa$  and zero velocity so as to approximate the conditions in T4 experiments in which the test section of the facility is evacuated to approximately 2 Torr.

The inflow conditions were set to approximate the flow in the T4 facility fitted with a Mach 5 contoured nozzle. The nozzle supply pressure was approximately  $P_s = 52MPa$  and total enthalpy was,  $H_s = 8.4MJ/kg$ . Details of the experiment are recorded in [15].

The test flow conditions, both in the shock-reflection region and the nozzle, were computed as quasi-steady flows. The nozzle supply conditions (behind the reflected shock) were estimated with the FORTRAN program "ESTC" [19] which incorporated an equilibrium model for air. From the shock reflection conditions, the gas expanded adiabatically (and in



chemical equilibrium) to the measured nozzle supply pressure of  $52\text{MPa}$ . Using these conditions, the flow at the exit plane of the nozzle was estimated with the quasi-one-dimensional program "NENZF" [20] in which the test gas consisted of a mixture of the species  $N_2$ ,  $N$ ,  $O_2$ ,  $O$ ,  $NO$ ,  $NO^+$  and  $e^-$ . The gas was assumed to be in chemical equilibrium at the nozzle throat but a finite rate chemistry model with 11 reactions was used in the expansion region of the nozzle.

The "steady" conditions at the end of the nozzle (and inlet to the combustor) were specified as free-stream velocity  $3670\text{ms}^{-1}$ , a static pressure of  $21.5\text{kPa}$ , a static temperature of  $1165\text{K}$ , and oxygen and nitrogen mass fractions of 0.2314 and 0.7686 respectively. Although the NENZF program determined a species mixture that included finite amounts of  $O$  and  $NO$ , only a nonreacting mixture of  $O_2$  and  $N_2$  was used in the SPARK-2D computations.

The "transient" inflow was constructed from the nozzle supply pressure trace shown in Figure 3, assuming a quasi-steady flow and using the ESTC and NENZF codes to compute the nozzle exit conditions for a number of values of  $P_s$ . The time evolution of  $P_s$  was then approximated by the curve fit

$$\begin{aligned} P_s &= P_{peak}(0.215 + 4.540t - 22.148t^3), 0 < t < 0.28, \\ &= P_{peak}(\exp(-0.775(t - 0.28))), 0.28 < t < 2.26, \end{aligned} \quad (7)$$

where  $P_{peak} = 62\text{MPa}$ ,  $t$  is in  $ms$  and  $P_s$  is in  $MPa$ . The conditions at the inlet to the scramjet combustor were then related to  $P_s$  with the following equations

$$P_{in}(\text{kPa}) = 0.435P_s - 1.55, \quad (8)$$

$$T_{in}(\text{K}) = 525P_{in}^{0.256}, \quad (9)$$

$$U_{in}(\text{ms}^{-1}) = 350T_{in}^{0.333}. \quad (10)$$

The histories of the inlet conditions are shown in Figure 8.

### 3.4. Numerical Damping

Some difficulty was experienced in starting the solution with such low pressure and large incident-shock Mach number (which was approximately 10 for Case 1). The difficulty appeared to be caused by the interaction of the strong incident shock structure with the newly forming recompression shock. To get the calculation started, the CFL number was linearly varied from 0.1 to 0.8 over the first 18000 time steps. For Cases 2,3,4 and 5, the coefficient for the artificial viscosity terms was set to a constant value of -1.0 while, for Cases 1 and 6, it was set to -1.2. To faithfully capture heat transfer, temperature smearing was not included.

### 3.5. Normalization Procedure for Transient Flow

The flow quantities,  $q(x, t)$ , computed in the transient Cases 2, 3 & 5 were normalized with upstream reference values to produce equivalent quasi-steady values,  $\hat{q}(x, t)$ . The particular transformation used, based on the "hypersonic equivalence principle" was

$$\hat{q}(x, t) = \frac{q(x, t)}{q(x_0, t - \tau_{delay})}, \quad (11)$$

where the time delay,  $\tau_{delay}$ , was given as the nominal transit time from the reference position

$$\tau_{delay} = \frac{x - x_0}{U_{in}}. \quad (12)$$

Essentially this means that individual parcels of fluid were followed downstream through the combustor and measured quantities were referenced to the parcels' initial states. (See, e.g., Section 4.8 of [4].)

## 4. RESULTS AND DISCUSSION

In previous studies of impulsively started flows [21] [22] [23] [24] one principal result has been the time taken for the flow to approach steady state. This establishment time  $\tau_e$  is usually combined with a characteristic velocity,  $U_c$ , and a length,  $L_c$ , to form the dimensionless parameter

$$G = \frac{U_c \tau_e}{L_c}, \quad (13)$$

which represents the ratio of the flow establishment time to the time for flow to proceed through the domain. For the flow features in the generic scramjet, such as boundary layers and recirculation regions,  $G$  will have different values. For the impulsively started flow over a flat plate, where the boundary layer is laminar and  $L_c$  is the distance from the start of the plate,  $G$  is approximately 3 [21]. When the boundary layer is turbulent  $G \simeq 2$ . For the wake of a sphere, with  $L_c$  as the length of the recirculation region, Holden [22] gives  $G \simeq 30$ , based on the pressure measurements and  $G \simeq 70$  based on heat transfer measurements.

In this section, six numerical simulations of the transient flow in a generic scramjet combustor will be examined with emphasis on the approach to steady state (or quasi-steady state as determined by the hypersonic equivalence principle). The following parameters will be used to determine flow establishment times: the boundary layer thicknesses at the end of the injector strut, the length of the recirculation region, the location of the recompression shock and, the pressure, heat flux and shear stress on the  $y = 0.02357m$  wall. The computation of the flow development for each of the cases was continued to a time of approximately  $1ms$  which is typical of the flow time in the current generation of pulsed-flow facilities.

#### 4.1. Overview of the Solutions

Figures 9 and 10 show the pressure fields for the short injector geometry with steady inflow (Case 1) and transient inflow (Case 2) respectively. Contour spacing is  $2kPa$ . These figures highlight the similarity between the steady inflow and the transient inflow solutions. The pressure distributions along the  $y = 0$  and  $y = 0.02357m$  walls are shown on the right side of each figure. Note that the stretching of the  $y$ -coordinate (by a factor of 5) changes the appearance of the shock and Mach angles.

At the start of the duct, there are a pair of weak shocks generated by the initially rapid growth of the boundary layer on the duct walls. Although not evident in the pressure field plots, boundary layers develop along the upper wall and the injector surface. The boundary layer on the injector separates at the step ( $x = 0.114m$ ) and reattaches to the  $y = 0$  boundary some distance downstream. The expansion from the corner of the injector, and the recompression shock formed near the end of the recirculation zone are clearly visible for both cases. Subsequent reflections of the recompression shock from the duct walls can be seen for  $t \geq 0.2ms$ .

The initial shock structure sweeping through the duct for  $t < 0.16ms$  is composed of an incident shock propagating downstream through the quiescent gas, a contact discontinuity separating the initial duct gas and the incoming test gas, and an upstream-facing shock decelerating the incoming test gas. Both the second-order and fourth-order MacCormack schemes experienced some difficulty with this strong shock structure and numerical oscillations are evident in the solutions for  $t < 0.20ms$ . However, it is expected that the solutions are reliable at later times.

The incident-shock position was identified as the point at which the wall pressure rose from (the initial value of)  $300Pa$  to  $800Pa$ . The position was recorded every  $100\mu s$  and the data points were then fitted with the straight line

$$x = v(t - t_0). \quad (14)$$

The values of  $v$  and  $t_0$  are given in Table 4. In all cases, the shock speed was virtually constant throughout the flow domain. However, the transient inflow cases (2,3 and 5) had a lower incident-shock speed than the steady inflow cases. For Cases 1 and 6, the position of the upstream-facing shock was identified as the point where the wall pressure crossed a  $35kPa$  threshold. The velocities for this shock are also given in Table 4.

As shown by the pressure contour plots and the wall pressure plots in Figures 9 and 10, the overall flow features of both steady inflow and transient inflow cases are similar. Although the starting shock structure took longer to exit the duct for the transient inflow (Case 2), the major steady-state features such as the boundary-layer interaction shocks, the

expansion fan and the recompression shock are in virtually the same places. The principal difference seems to be the average level of the duct pressure which can be seen relaxing in the wall pressure plots of Figure 10.

The effect of including the complete injector strut in the computational model can be seen in Figure 11, which shows a few frames from Cases 3 and 5. The frames are placed back to back and the times have been chosen to show approximately the same stages of development. However, the instantaneous inflow conditions are not exactly the same in each pair of frames. The major differences are the strong shock and expansion propagating from the front of the long injector. Also, the shock propagating from the leading edge of the  $y = 0.02357m$  wall is stronger than the boundary-layer interaction shocks seen in the short injector simulations. After reflecting from the injector strut and then the duct wall, this leading-edge shock interacts with the expansion fan propagating from the base of the strut.

Since there is only a small difference between the long-injector and short-injector simulations, the following discussion will concentrate on the details of the short-injector simulations.

#### 4.2. Injector-Strut Boundary Layer

For the short injector simulations, the boundary layer along the strut surface closely approximates the ideal flat-plate boundary layer, the main difference being the boundary-layer interaction shock striking the strut surface at  $x \simeq 0.09m$ . This weak shock did not seem to affect the flow profiles within the boundary layer at the end of the strut ( $x = 0.114m$ ) where the following thicknesses were calculated:

- total boundary layer thickness,  $\delta$ ; the  $y$ -distance from the strut surface to 0.99 of the local free-stream velocity  $u_e$ ,
- the displacement thickness

$$\delta^* = \int \left( 1 - \frac{\rho u}{\rho_e u_e} \right) dy, \quad (15)$$

- the momentum thickness

$$\theta = \int \frac{\rho u}{\rho_e u_e} \left( 1 - \frac{u}{u_e} \right). \quad (16)$$

The temporal development of  $\delta$ ,  $\delta^*$  and  $\theta$  is shown in Figure 12. For the steady inflow, the thicknesses approach to within 2% of steady state values by  $t = 0.23 - 0.26ms$ . If the approach to steady state begins with the passage of the upstream-facing shock, these times give  $G \simeq 7$  which is roughly double the value expected for a laminar boundary layer in shock-tube flow [21]. This result seems to indicate that the incident shock structure, including the

contact surface and the upstream facing shock, interferes with the establishment processes and delays the approach to steady state.

The steady value of  $\delta = 1.49mm$  is close to the value of  $1.45mm$  obtained with the "reference temperature" relations of Eckert [25] and Equation (7.53) in White [26]. This agreement provides some confidence that the viscous effects have been adequately resolved. Also, the flat plate transition data from He & Morgan [27] indicate that transition to a turbulent boundary layer would be expected after a distance of approximately  $0.25m$ .

For the transient inflow cases, the approach to steady state is qualitatively different and, at late times, there is a slight growth in each of the thicknesses as a consequence of the relaxation of the free-stream pressure (and hence density).

#### 4.3. Recirculation Region

The form of the velocity field in the recirculation region at the base of the strut appeared to be insensitive to the transient inflow. Figure 13 shows the velocity field in the recirculation region for Cases 2 and 3. The symmetry plane boundary condition in Case 3 allows a stronger vortex to form closer to the strut base. The pressures along the  $y = 0$  line in the recirculation region are shown in Figure 14 at selected times.

The length of the recirculation region, as measured by the position of the stagnation point near the  $y = 0$  boundary, is shown in Figure 15. At late times, both the steady inflow and the relaxing inflow traces reach steady values. The steady state lengths are  $L_r = 9.5, 8.3, 10.1$  and  $10.8mm$  for Cases 1, 2, 3 and 6 respectively, which means that (a) the symmetry plane cases have longer recirculation zones than the solid wall cases and (b) the transient inflow cases have slightly shorter lengths than their steady inflow counterparts. Based on  $L_r$  for steady inflow, the base flow establishes in a dimensionless time  $G \simeq 146$  ( $t = 0.419ms$ ) for the solid wall (Case 1) and  $G \simeq 83$  ( $t = 0.283ms$ ) for the symmetry plane (Case 6).

Also shown in Figure 15 is the length of the recirculation region along the line  $y = 0.0025m$  which is half way up the base of the strut. This length was determined by computing the vertical mass flux

$$\dot{m}_y = \int \rho u_y dx, \quad (17)$$

and finding the  $x$ -location where  $\dot{m}_y$  became zero. This measure showed the same trends as the stagnation point measurement except that  $G \simeq 64$  ( $t = 0.229ms$ ) for the symmetry plane (Case 6).

#### 4.4. Recompression Shock

Figure 16 shows the pressure distributions along the  $y = 0$  plane for Cases 1 and 2.

The recompression shock is rather smeared and appears as the gradual pressure rise from  $x \simeq 0.12m$  to  $x \simeq 0.13m$ . Observe that the pressure distributions for the transient inflow (Case 2) collapse onto the one curve when they are normalized using the procedure discussed in Section 3.5.

The shock position along a line through the midpoint of the strut base ( $y = 0.0025m$ ) is plotted against time in Figure 17. The shock position was taken to be the grid location at which the pressure rises to 25% of the inlet pressure. Based on the length of the recirculation zone the nondimensional establishment time  $G \simeq 140$  ( $t = 0.402ms$ ) and  $G \simeq 80$  ( $t = 0.273ms$ ) for Cases 1 and 6 respectively.

#### 4.5. Wall Loads

The shear stress and heat flux were monitored at selected points along the  $y = 0.02357m$  wall. The shear stress coefficient is given by

$$C_f = \frac{\mu \left| \frac{\partial u_x}{\partial y} \right|_{wall}}{\frac{1}{2} \rho_{in} u_{in}^2}, \quad (18)$$

and the heat flux by the Stanton number

$$C_h = \frac{k \left| \frac{\partial T}{\partial y} \right|_{wall}}{\rho_{in} u_{in} C_p (T_{aw} - T_w)}, \quad (19)$$

where the normal derivatives of the velocity and temperature were approximated by differences at the first node off the wall. The viscosity was evaluated at the wall temperature using Sutherland's formula and  $\rho_{in}$  and  $u_{in}$  are inlet conditions computed with the time delay specified in Equation (12). Thermal conductivity  $k$  was obtained assuming  $C_p = 1004 J/kg/K$  and Prandtl number  $Pr \equiv \mu C_p / k = 0.71$ . The adiabatic wall temperature was obtained from

$$T_{aw} = T_{in} \left[ 1 + \sqrt{Pr} \frac{(\gamma - 1)}{2} M_{in}^2 \right]. \quad (20)$$

The development of these parameters at  $x = 0.114m$  and  $x = 0.5m$  is shown in Figures 18 and 19 respectively. Results for the steady inflow cases exhibit an approach to steady state at both locations. The normalization of the transient inflow measurements is not entirely successful as the values of both  $C_f$  and  $C_h$  settle to a constant rate of growth after some start-up period.

Normalized pressure histories at  $x = 0.114m$  and  $0.50m$  wall are shown in Figures 18(c) and 19(c) for completeness. There is only a slight variation in the traces for the two transient inflow cases indicating that the normalization works well for pressures. The slight variation may be caused by the use of the constant value  $U_c = 3670ms^{-1}$  in Equation (12).

#### 4.6. (x,t)-Diagrams

The time for wall pressure, shear stress and heat transfer to reach steady state at a number of x-locations along the  $y = 0.02357m$  wall is shown in Figures 20, 21 and 22 respectively. An average of each quantity between times  $t = 0.7ms$  and  $0.8ms$  was used as the steady value and the settling time  $t_e$  determined such that the flow quantity remains within 2% of the steady value for  $t_e < t < 0.7ms$ . The establishment time is then given as  $\tau_e = t_e - t_{uf}$  where  $t_{uf}$  is the arrival time of the upstream-facing shock. Only the steady inflow cases (1 and 6) are considered, since a consistent establishment criterion was not available for the transient inflow cases.

The wall pressure generally settles more quickly than shear stress or heat transfer and has a dimensionless establishment time of  $G = \tau_e U_c / x \simeq 0.9$  for  $x > 0.2m$ . However, the establishment is significantly delayed where the relatively weak boundary-layer-interaction shocks strike the wall at  $x \simeq 0.09m$  and  $0.18m$ . The pressure measurement does not settle at all where the relatively strong recompression shock strikes the wall at  $x \simeq 0.3m$ .

The establishment times for the shear stress are nearly the same as those for the heat transfer and, for  $x > 0.4m$ , can be approximated by  $G \simeq 3$ . A similar delay after the passage of the starting pulse was observed in the experimental measurements of East *et al.* [24]. For  $x < 0.3$ , the delay beyond the flat plate value of  $G \simeq 3$  is significant.

#### 5. CONCLUSION

In order to study the establishment of the major flow features in a generic scramjet combustor, several numerical simulations were analysed. Of particular interest was the effect of a transient relaxing inflow condition as found in a reflected-shock tunnel which has been operated in an undertailored mode.

From the numerical point of view, the simulations were particularly demanding and much of the interesting phenomena (such as turbulent mixing and chemistry) was omitted from these simulations. These issues will be addressed in a future study. The finite-difference scheme generally performed well but encountered difficulty with the very strong shock interactions and tended to produce oscillatory solutions at early times. With an incident-shock Mach number of approximately 10, these oscillations were not unexpected. An "upwinding" scheme (available in another version of the code) may better cope with the strong shocks.

From the experimental point of view, it appears that the correlations available in the literature are adequate for predicting the establishment times for the flow features of the model if the inflow conditions are steady and allowance is made for the passage of the starting pulse [24]. For the relaxing flow, there are perturbations outside the 2% error band for a

significantly longer time but these perturbations are probably smaller than the measurement uncertainty in the shock tunnel experiment. Hence, relaxing test flow with a duration of the order of a few hundred microseconds is probably adequate for establishing flow in moderate sized scramjet models if the recirculating zones are not too large. The establishment time for turbulent jet mixing in the presence of combustion needs to be examined.

The effect of the relaxing inflow conditions of the undertailored reflected-shock tunnel seem not to affect the overall pressure fields within the model nor the length of the recirculation region to any great extent. However, the relaxing flow does affect features such as the heat transfer and wall shear stress. It may also be expected to affect the chemical reaction rates which will scale as  $\rho L_c$  and  $\rho^2 L_c$  for two-body and three-body reactions respectively.



## References

- [1] R. J. Stalker. Hypervelocity aerodynamics with chemical nonequilibrium. *Annual Review of Fluid Mechanics*, 21:37-60, 1989.
- [2] J. P. Drummond, M. H. Carpenter, D. W. Riggins, and M. S. Adams. Mixing enhancement in a supersonic combustor. AIAA Paper 89-2794, 1989.
- [3] G. B. Northam and et al. Evaluation of parallel injector configurations for supersonic combustion. AIAA Paper 89-2525, 1989.
- [4] J. D. Anderson. *Hypersonic and High Temperature Gas Dynamics*. McGraw-Hill, New York, 1989.
- [5] J. P. Drummond, R. C. Rogers, and M. Y. Hussaini. A detailed numerical model of a supersonic reacting mixing layer. AIAA Paper 86-1427, 1986.
- [6] J. P. Drummond. A two-dimensional numerical simulation of a supersonic, chemically reacting mixing layer. NASA Technical Memorandum 4055, 1988.
- [7] R. C. Rogers and E. H. Weidner. Numerical analysis of the transient flow from a shock tunnel facility. AIAA Paper 88-3261, 1988.
- [8] R. G. Morgan and et al. Shock tunnel studies of scramjet phenomena. NASA Contractor Report 181721, 1988.
- [9] J. Tamagno and et al. Results of preliminary calibration tests in the gasl hypulse facility. GASL Technical Report 308, General Applied Science Laboratories, Ronkonkoma, New York, 1989.
- [10] C. E. Wittliff, M. R. Wilson, and A. Hertzberg. The tailored-interface hypersonic shock tunnel. *J. Aerospace Sci.*, 26:219-228, 1959.
- [11] C. E. Smith. The starting process in a hypersonic nozzle. *Journal of Fluid Mechanics*, 24:625-640, 1966.
- [12] L. Davies and J. L. Wilson. Influence of reflected shock and boundary-layer interaction on shock-tube flows. *The Physics of Fluids Supplement 1*, 1969.
- [13] R. J. Stalker and K. C. A. Crane. Driver gas contamination in a high enthalpy reflected shock tunnel. *AIAA. Journal*, 16(3):277-279, 1978.

- [14] R. J. Stalker. A study of the free-piston shock tunnel. *AIAA Journal*, 5(12):2160-2165, 1967.
- [15] P. A. Jacobs and et al. Preliminary calibration of a generic scramjet combustor. Department of Mechanical Engineering Report in preparation, University of Queensland, 1990.
- [16] G. O. Roberts. Computational meshes for boundary layer problems. In *Lecture Notes in Physics*, 8, pages 171-177. Springer-Verlag, 1971.
- [17] D. A. Anderson, J. C. Tannehill, and R. H. Pletcher. *Computational Fluid Mechanics and Heat Transfer*. Hemisphere, New York, 1984.
- [18] P. D. Thomas, M. Vinokur, R. Bastianon, and R. J. Conti. Numerical solution for the three-dimensional hypersonic flow field of a blunt delta body. *AIAA Journal*, 10:887-894, 1972.
- [19] M. K. McIntosh. Computer program for the numerical calculation of frozen and equilibrium conditions in shock tunnels. Technical report, Australian National University, 1968.
- [20] J. A. Lordi, R. E. Mates, and J. R. Moselle. Computer program for the numerical solution of nonequilibrium expansions of reacting gas mixtures. NASA Contractor Report 472, 1966.
- [21] W. R. Davies and L. Bernstein. Heat transfer and transition to turbulence in the shock-induced boundary layer on a semi-infinite flat plate. *Journal of Fluid Mechanics*, 36(1):87-112, 1969.
- [22] M. S. Holden. Establishment time of laminar separated flows. *AIAA Journal*, 9(11):2296-2298, 1971.
- [23] E. J. Felderman. Heat transfer and shear stress in the shock-induced unsteady boundary layer on a flat plate. *AIAA Journal*, 6(3):408-412, 1968.
- [24] R. A. East, R. J. Stalker, and J. P. Baird. Measurements of heat transfer to a flat plate in a dissociated high-enthalpy laminar air flow. *Journal of Fluid Mechanics*, 97(4):673-699, 1980.
- [25] E. R. G. Eckert. Engineering relations for friction and heat transfer to surfaces in high velocity flow. *Journal of the Aeronautical Sciences*, 22(8):585-587, 1955.

- [26] F. M. White. *Viscous Fluid Flow*. McGraw-Hill, New York, 1974.
- [27] Y. He and R. G. Morgan. Transition of compressible high enthalpy boundary layer flow over a flat plate. In *Tenth Australasian Fluid Mechanics Conference, Melbourne.*, 1989.

Table 1: Cases Considered in this Study

| Case | Geometry |                  | Inflow for $t > 0$ | Spatial Differencing |
|------|----------|------------------|--------------------|----------------------|
|      | injector | $y = 0$ boundary | steady/transient   |                      |
| 1    | short    | cold wall        | steady             | 2nd order            |
| 2    | short    | cold wall        | transient          | 2nd order            |
| 3    | short    | symmetry plane   | transient          | 2nd order            |
| 4    | long     | symmetry plane   | steady             | 4th order            |
| 5    | long     | symmetry plane   | transient          | 4th order            |
| 6    | short    | symmetry plane   | steady             | 2nd order            |

Table 2: Grid Generation Parameters for Cases 1, 2, 3, and 6

(a)  $y$ -grid

| Zone | $y_a$<br>(m) | $y_b$<br>(m) | $\alpha$ | $\beta$ | $N$ | $\Delta y_{\min}$<br>(m) |
|------|--------------|--------------|----------|---------|-----|--------------------------|
| 1    | 0.005        | 0.0          | 0.5      | 1.113   | 34  | $50 \times 10^{-6}$      |
| 2    | 0.02357      | 0.005        | 0.5      | 1.0307  | 51  | $50 \times 10^{-6}$      |

(b)  $x$ -grid

| Zone | $x_a$<br>(m) | $x_b$<br>(m) | $\alpha$      | $\beta$ | $N$ | $\Delta x_{\min}$<br>(m) |
|------|--------------|--------------|---------------|---------|-----|--------------------------|
| 1    | 0.1          | 0.0          | 0.5           | 1.153   | 40  | 0.001                    |
| 2    | 0.114        | 0.1          | 0.0           | 1.1495  | 22  | 0.00025                  |
| 3    | 0.114        | 0.124        | equal spacing |         | 40  | 0.00025                  |
| 4    | 0.124        | 0.168        | 0.0           | 1.042   | 30  | 0.00025                  |
| 5    | 0.50         | 0.168        | equal spacing |         | 111 | 0.00299                  |

Table 3: Grid Generation Parameters for Cases 4 and 5

(a)  $y$ -grid for  $x > -0.10964m$

| Zone | $y_a$<br>(m) | $y_b$<br>(m) | $\alpha$ | $\beta$ | $N$ | $\Delta y_{\min}$<br>(m) |
|------|--------------|--------------|----------|---------|-----|--------------------------|
| 1    | 0.02357      | 0.0050       | 0.5      | 1.05    | 70  | $51 \times 10^{-6}$      |
| 2    | 0.0050       | 0.0          | 0.5      | 1.10    | 30  | $53 \times 10^{-6}$      |

(b)  $y$ -grid for  $-0.138m \leq x \leq -0.10964m$  and  $\bar{x} = (x + 0.138)/0.02836$

| Zone | $y_a$<br>(m)     | $y_b$<br>(m)             | $\alpha$ | $\beta$ | $N$ | $\Delta y_{\min}$<br>(m) |
|------|------------------|--------------------------|----------|---------|-----|--------------------------|
| 1    | 0.02357          | $0.0050 \bar{x}$         | 0.5      | 1.05    | 70  | $65 \times 10^{-6}$      |
| 2    | $0.0050 \bar{x}$ | $-0.00639 (1 - \bar{x})$ | 0.5      | 1.10    | 30  | $67 \times 10^{-6}$      |

(c)  $x$ -grid

| Zone | $x_a$<br>(m) | $x_b$<br>(m) | $\eta_0$                                   | $\beta$ | $N$ | $\Delta x_{\min}$<br>(m) |
|------|--------------|--------------|--|---------|-----|--------------------------|
| 1    | -0.0813      | -0.138       | -0.1096                                    | 1.5     | 30  | 0.00173                  |
| 2    | 0.0813       | -0.0813      | 0.0  | 3.5     | 110 | 0.00093                  |
| 3    | 0.1467       | 0.0813       | 0.114                                      | 7.0     | 80  | 0.00017                  |
| 4    | 0.2044       | 0.1467       | $\frac{\Delta x_i}{\Delta x_{i-1}} = 1.01$ |         | 19  | 0.00277                  |
| 5    | 0.50         | 0.2044       |  |         | 89  | 0.00332                  |

Table 4: Incident Shock (is) Speed and Upstream-Facing Shock (ufs) Speed as defined by Equation (14).

| Case | $v_{is}$<br>(m/ms) | $t_{is}$<br>(ms) | $v_{ufs}$<br>(m/ms) | $t_{ufs}$<br>(ms) |
|------|--------------------|------------------|---------------------|-------------------|
| 1    | 3.68               | 0                | 2.83                | 0                 |
| 2    | 2.96               | 0                | -                   | -                 |
| 3    | 2.97               | 0                | -                   | -                 |
| 4    | 3.72               | 0.0350           | -                   | -                 |
| 5    | 2.97               | 0.0466           | -                   | -                 |
| 6    | 3.71               | 0                | 2.83                | 0                 |

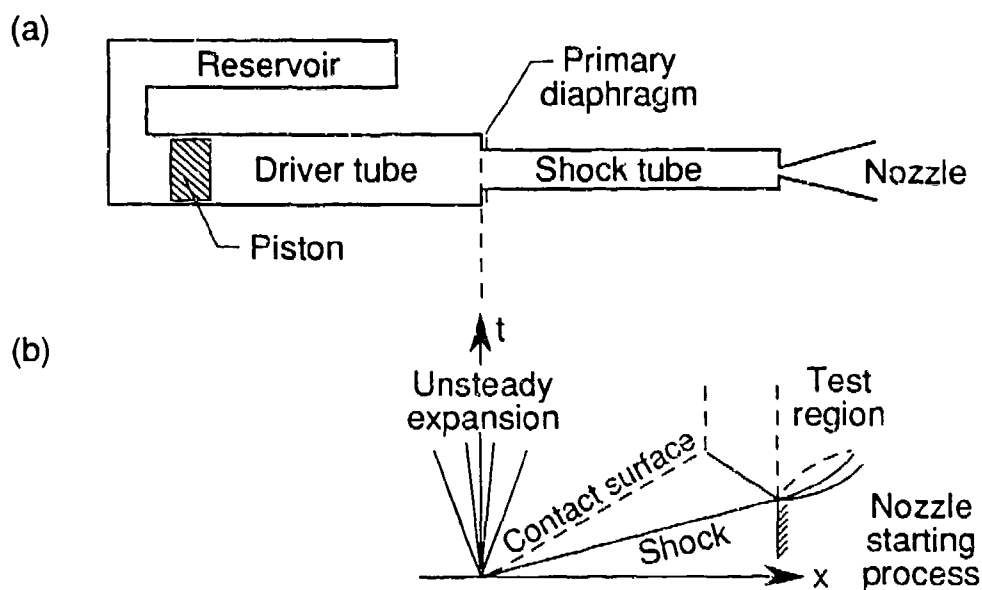


Figure 1: Free-piston driven reflected-shock tunnel.

(a) Facility schematic.

(b) Distance-time wave diagram after primary diaphragm rupture.

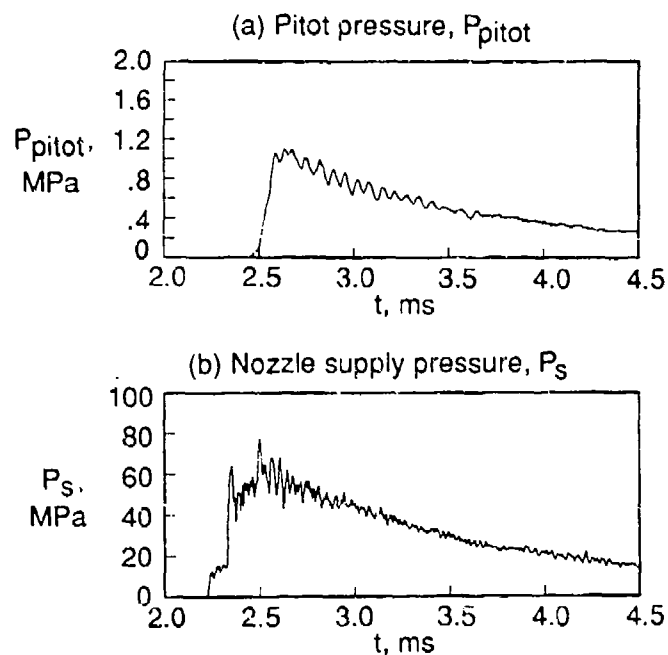


Figure 2: Typical pressure histories for the T4 shock tunnel.

(a) Pitot pressure at the exit plane of a Mach 5 nozzle.

(b) Nozzle supply pressure.

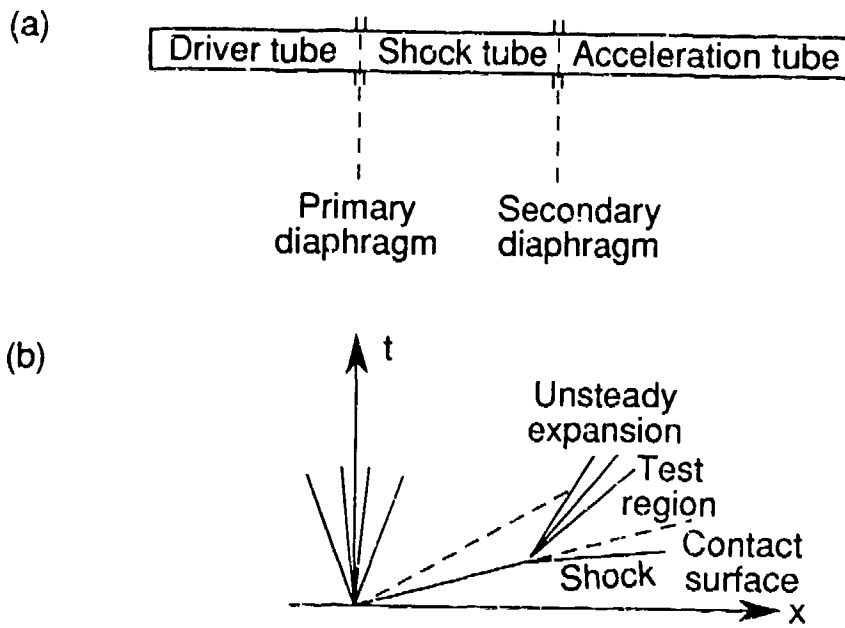


Figure 3: Expansion tube facility (a) and wave diagram (b).

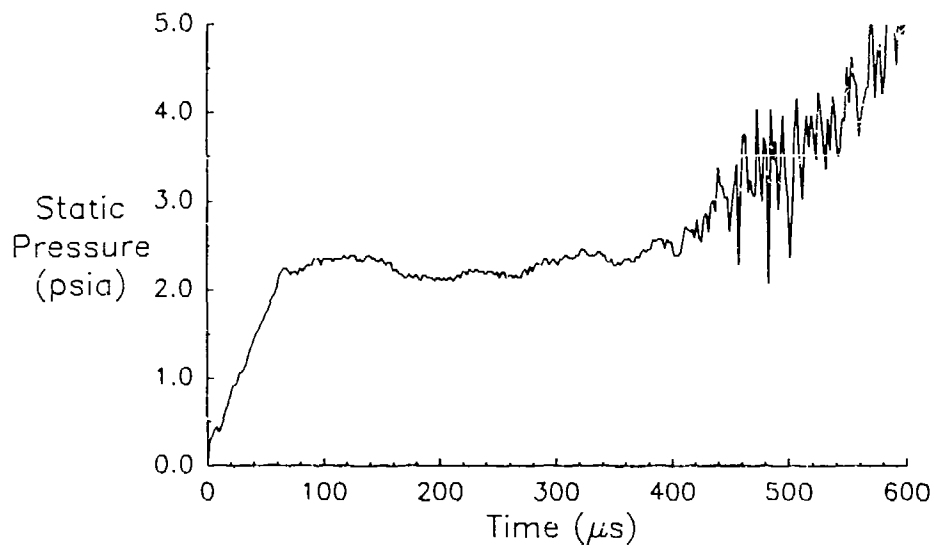


Figure 4: Typical static pressure in the HYPULSE facility.



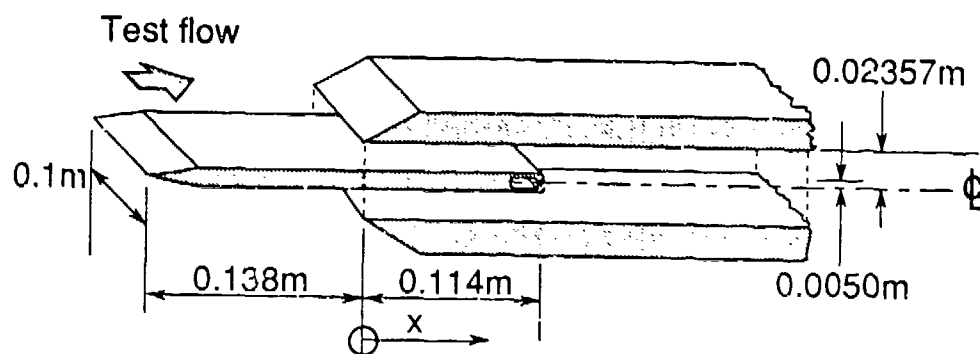


Figure 5: A generic scramjet combustor with centrally located fuel injector strut.

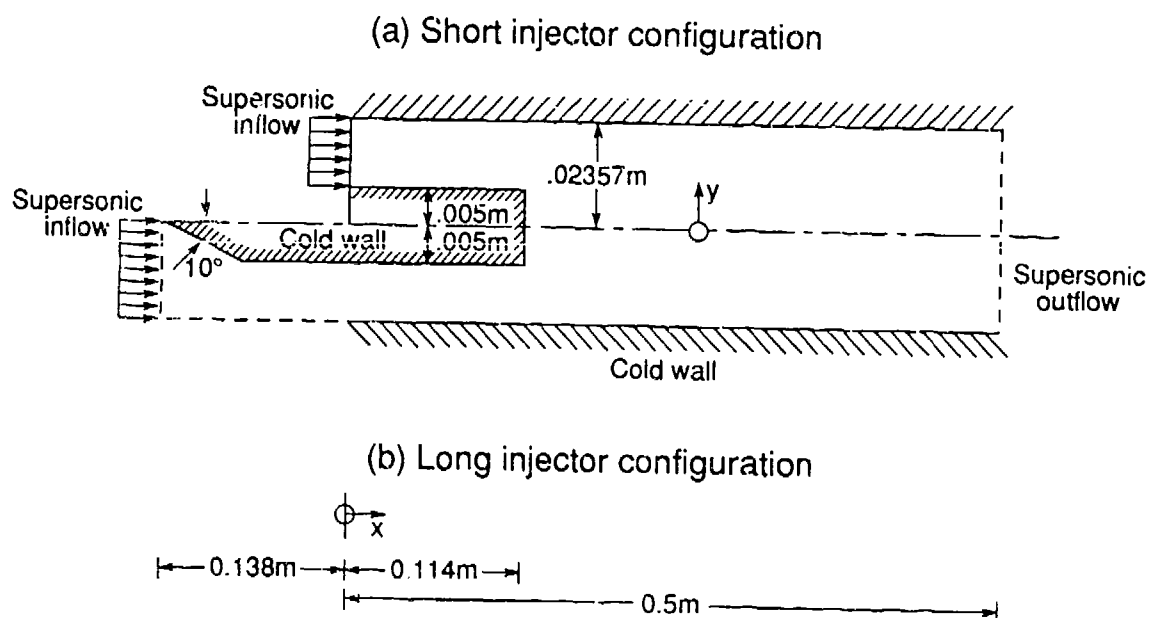


Figure 6: Combustor geometry used in the computations.

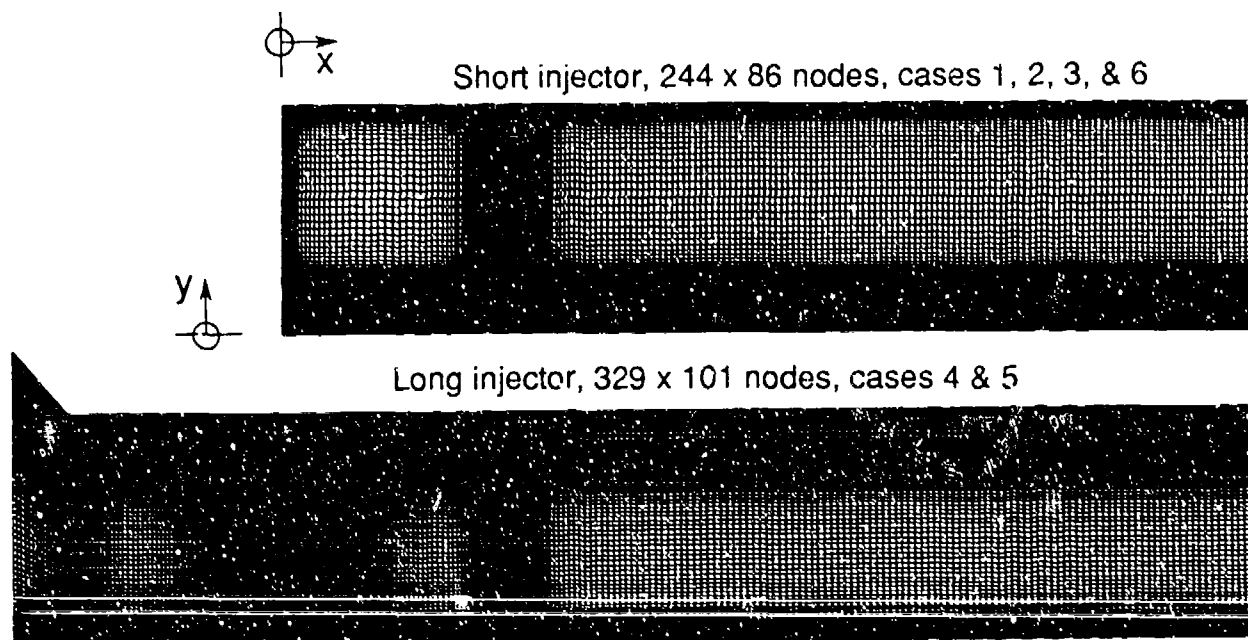


Figure 7: Grids used for the calculations. Note that the y-scale is magnified by a factor of five.

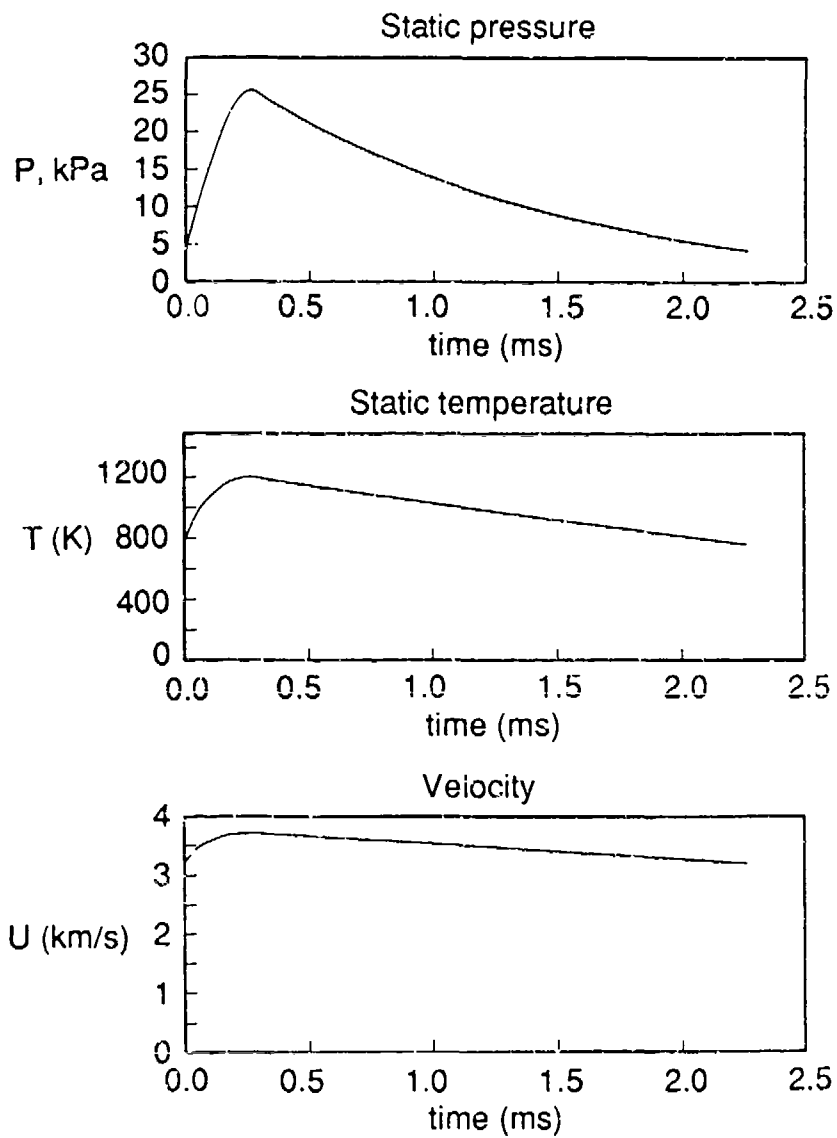


Figure 8: Transient inlet conditions as specified by equations (7) - (10).

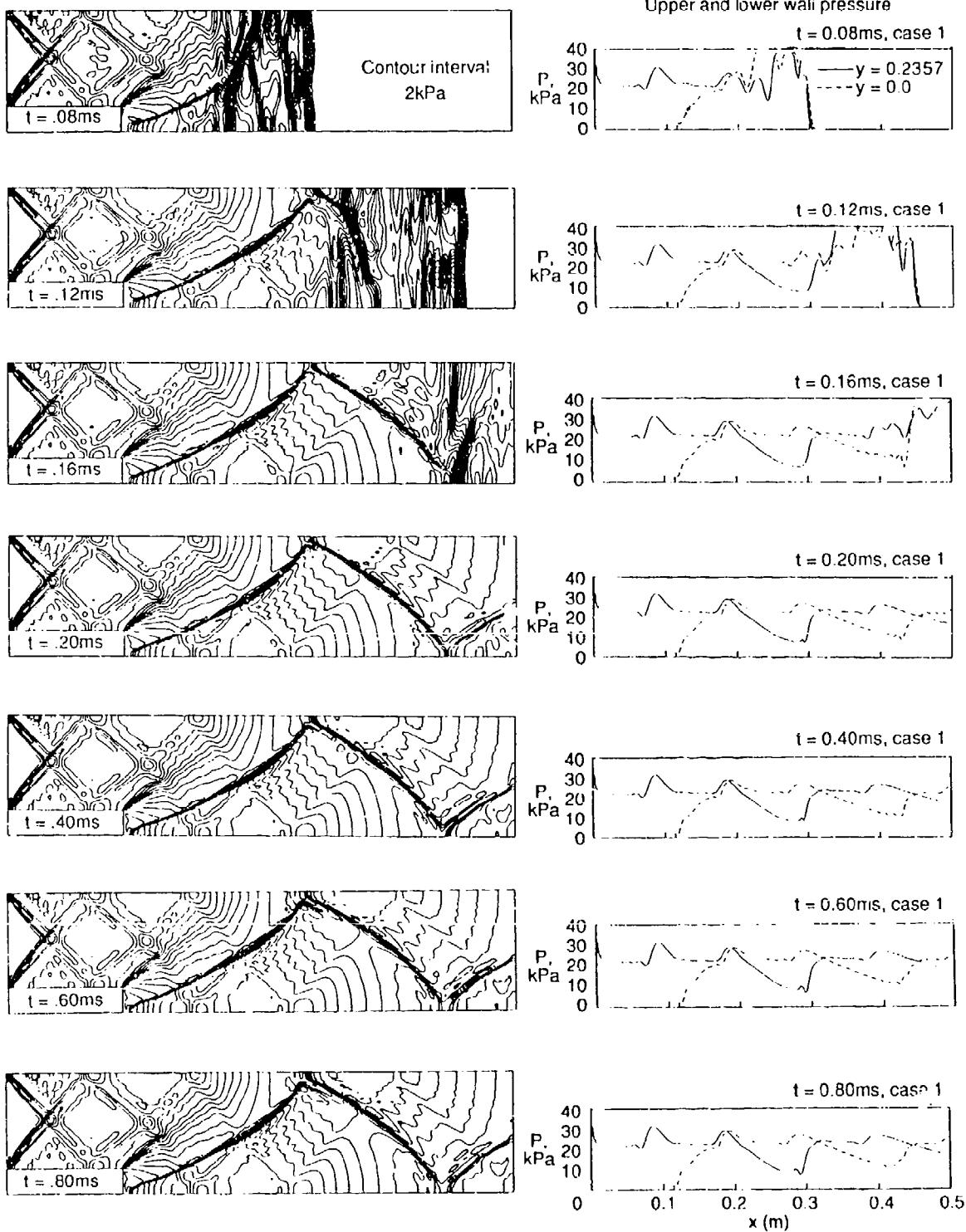


Figure 9: Evolution of the pressure field for Case 1 (steady inflow) at selected times.

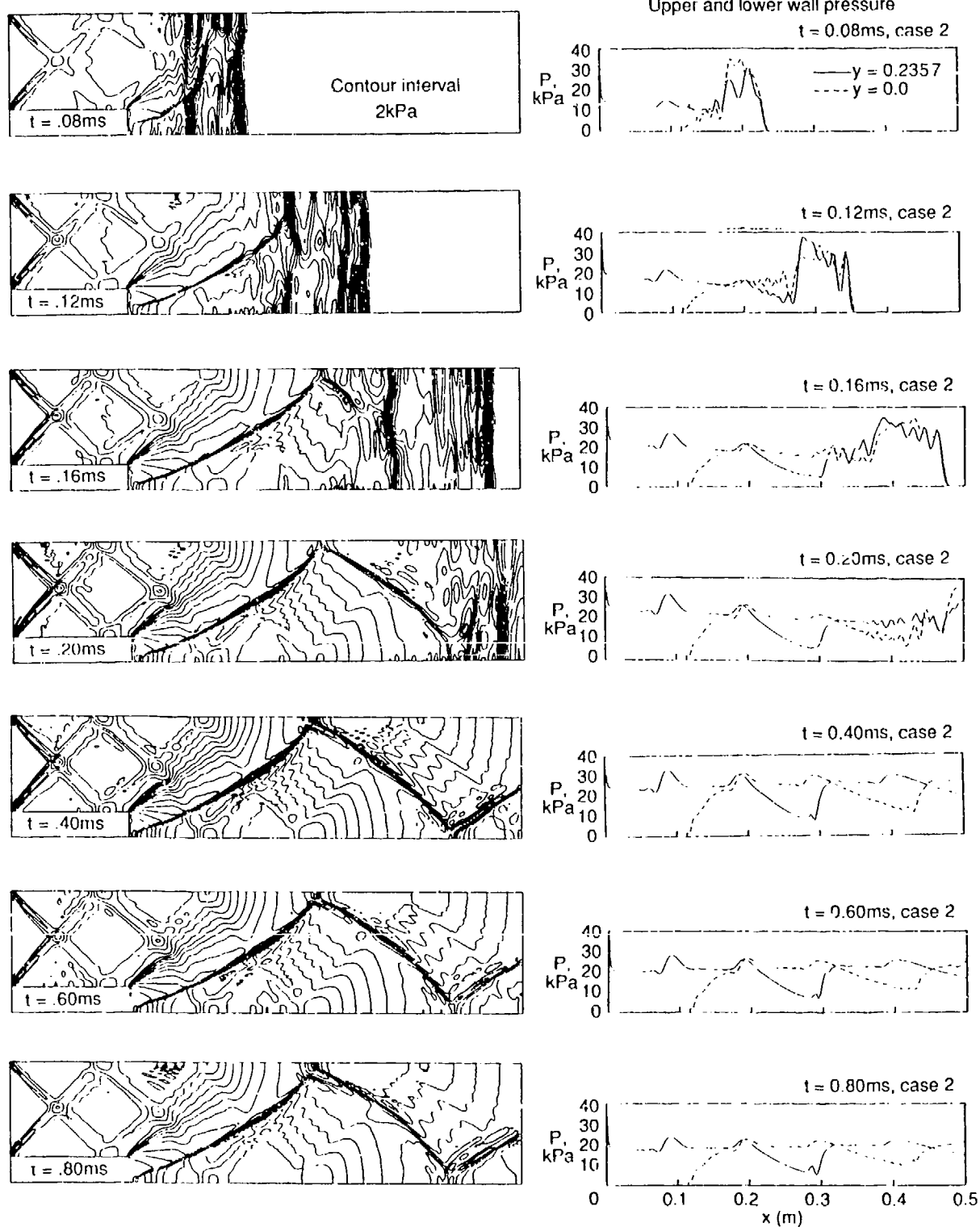


Figure 10: Evolution of the pressure field for Case 2 (transient inflow) at selected times.

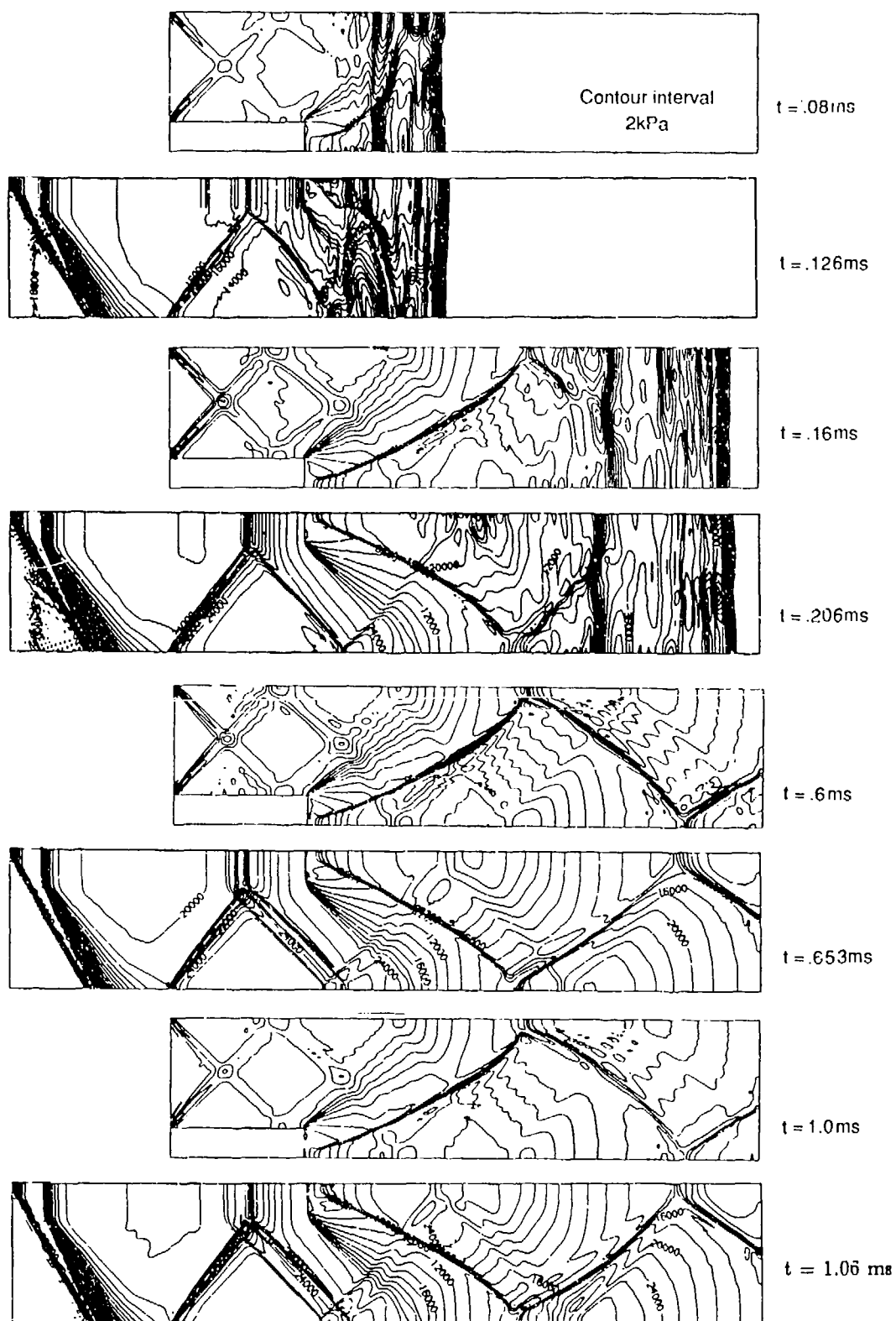


Figure 11: Comparison of pressure fields for Cases 3 and 5.

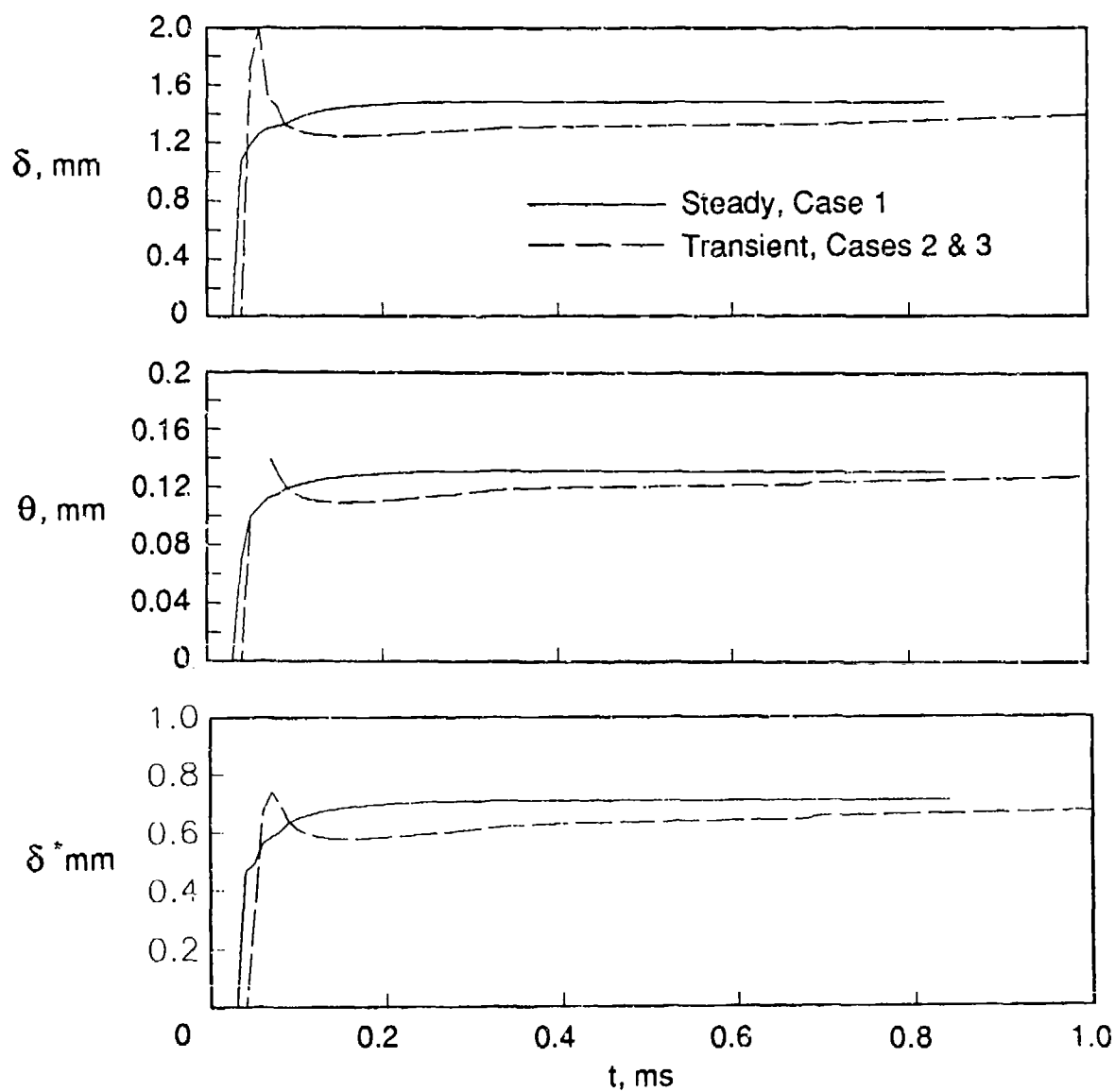
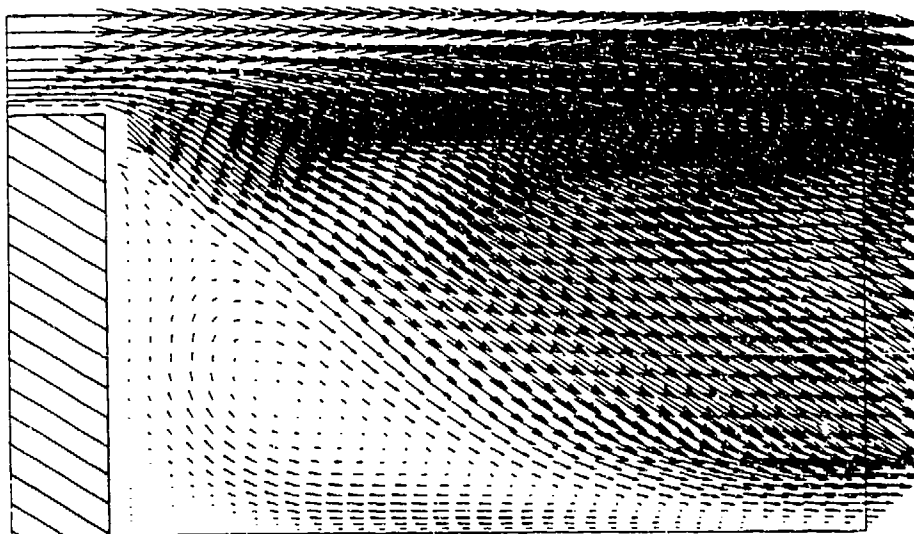


Figure 12: Development of the boundary layer thickness at the end of the short injector strut ( $x = 0.114m$ ,  $y = 0.005m$ ).

Case  
2



Case  
3

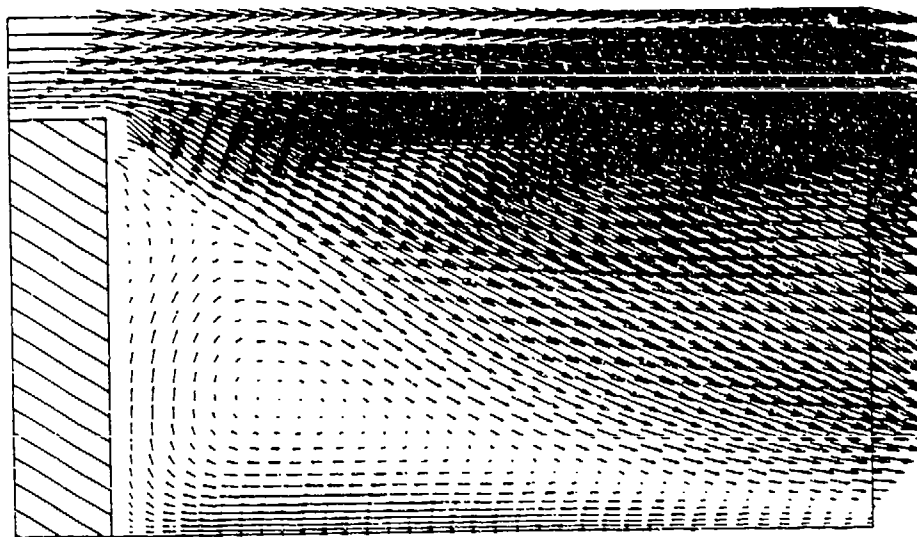


Figure 13: Velocity field in the base region of the injector at  $t = 0.6ms$  for Cases 2 and 3.



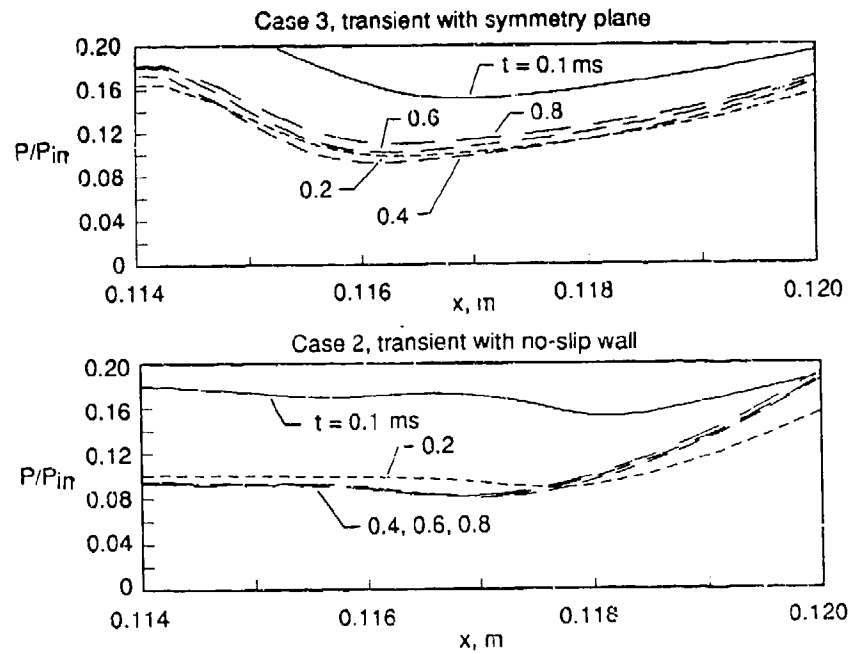


Figure 14: Pressure distributions along  $y = 0$  near the base of the injector for Cases 2 and 3.

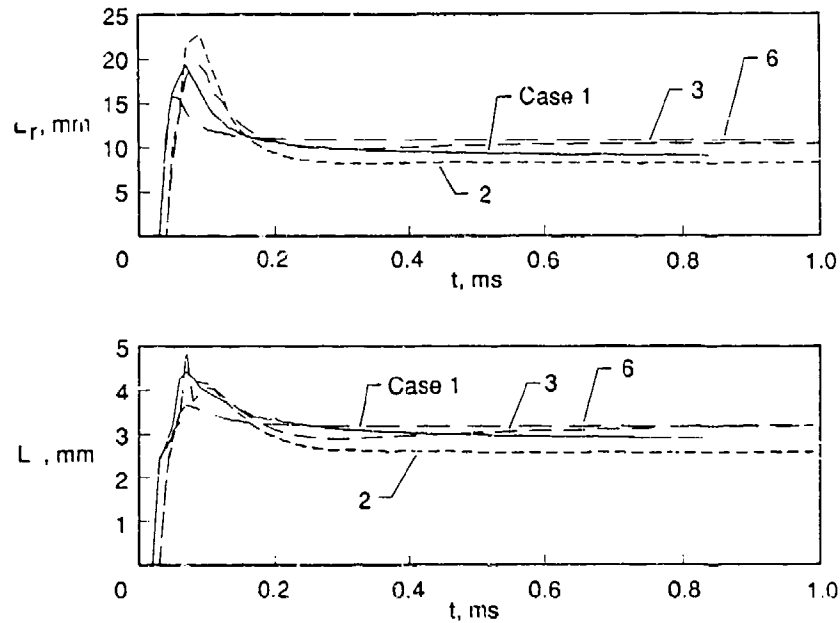


Figure 15: Length of the recirculation region.

(a)  $L_r$  identified by the stagnation point location.

(b) length identified by a zero-crossing of the vertical mass flux along the line  $y = 0.0025m$ .

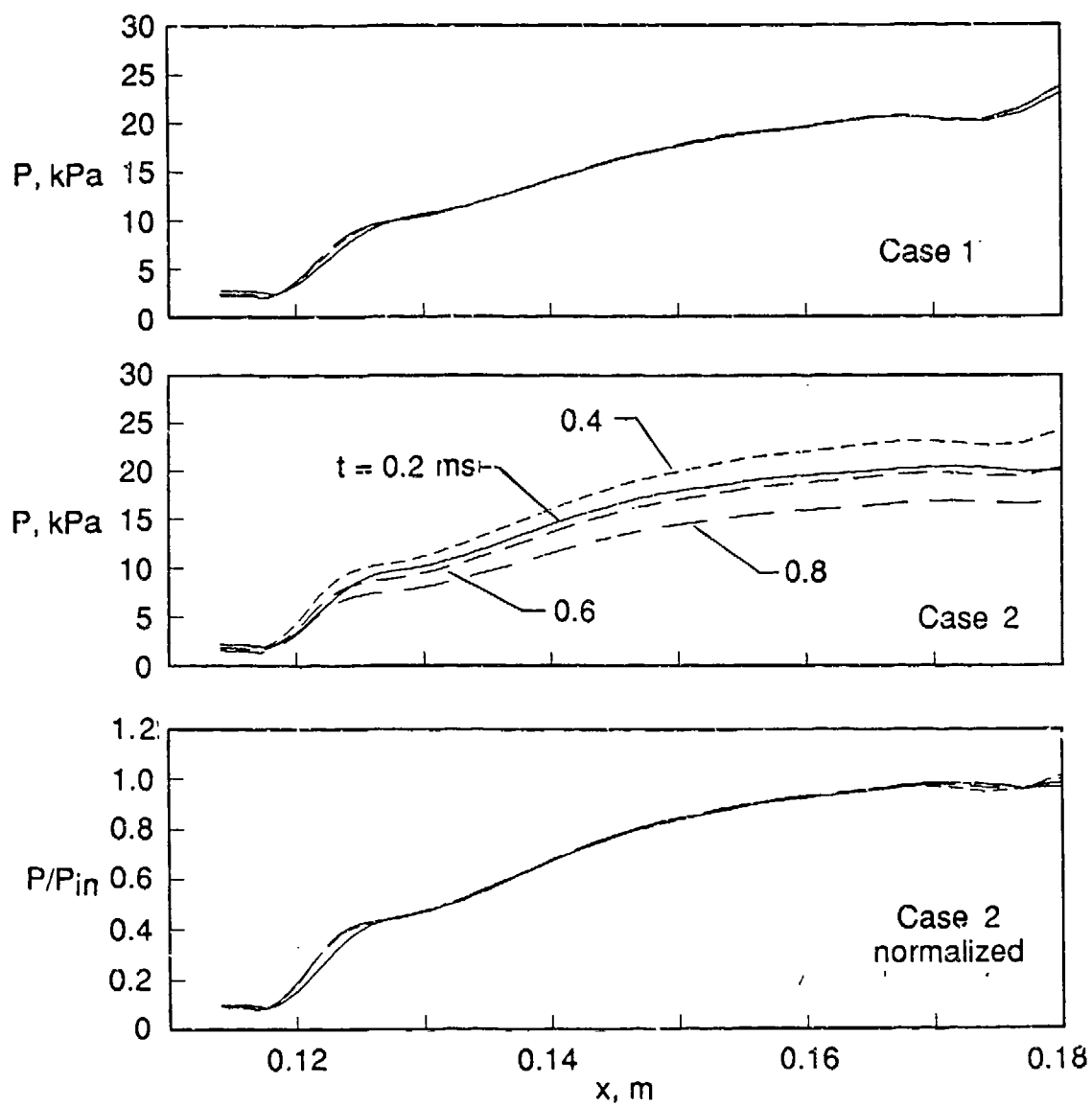


Figure 16: Pressures distribution at  $y = 0$  downstream of the injector for Cases 1 and 2.

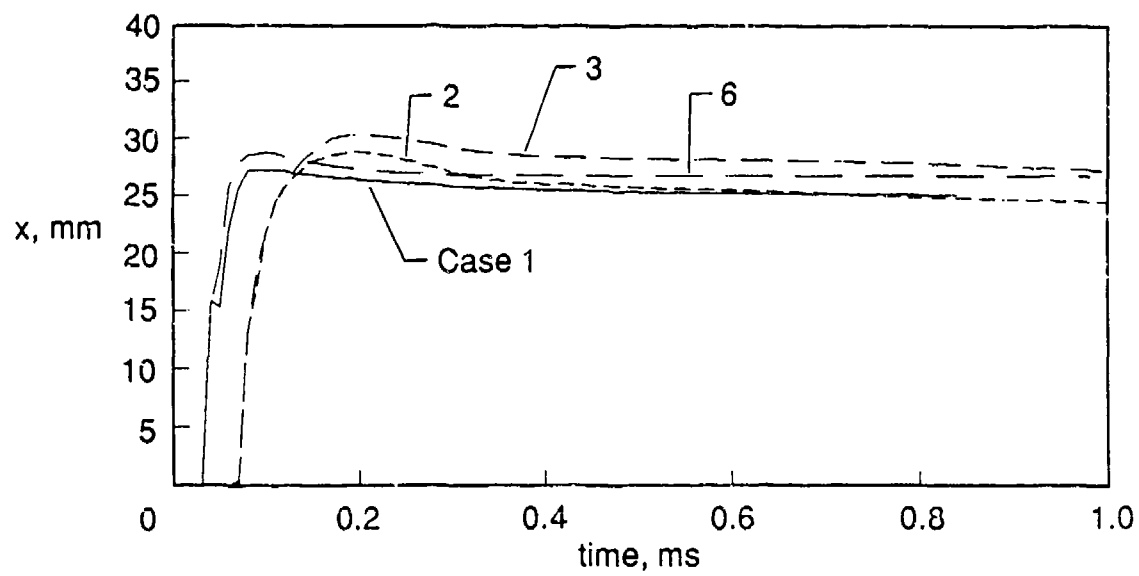


Figure 17: Location of the recompression shock along the line  $y = 0.0025m$ .

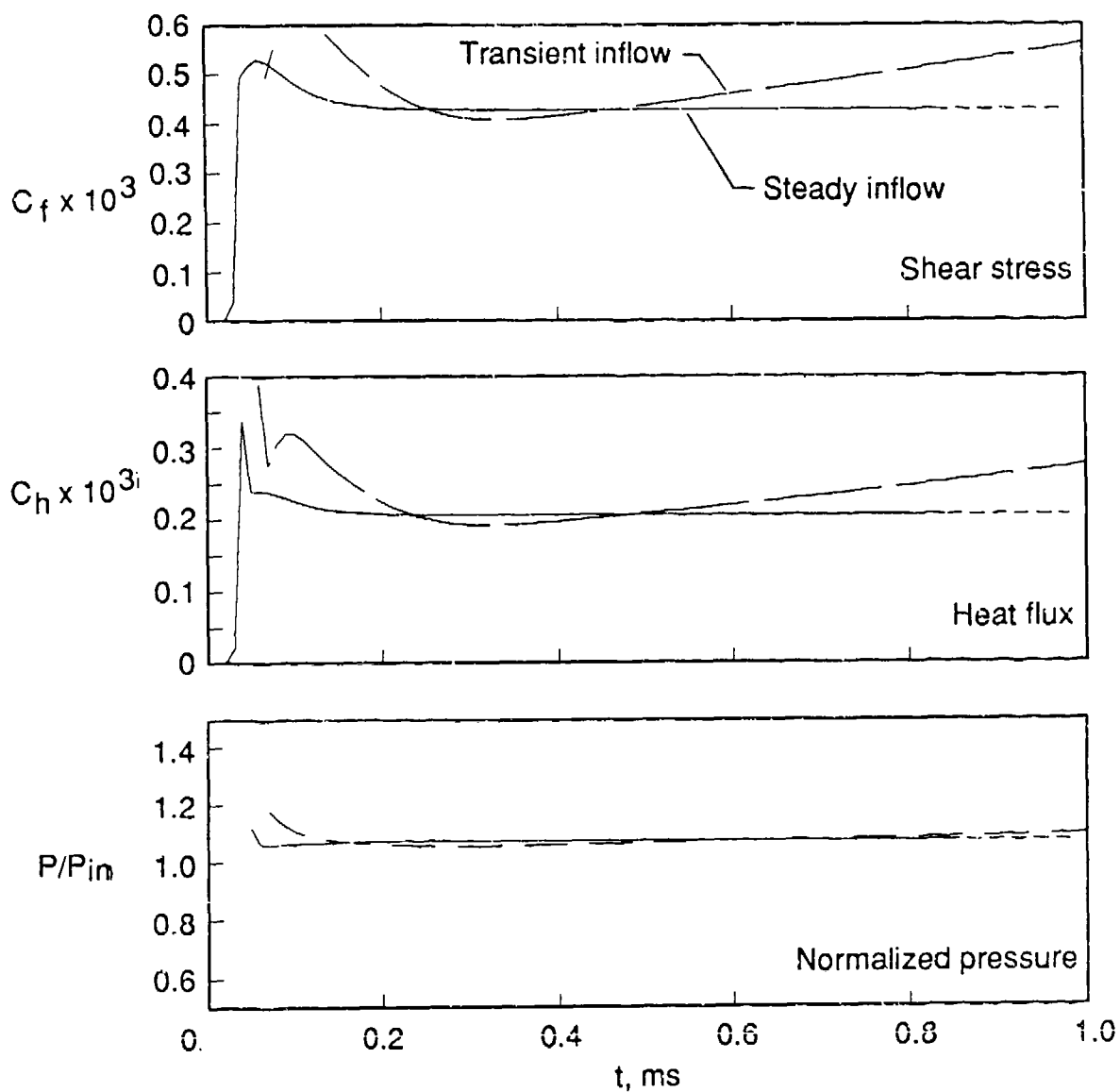


Figure 18: Comparison of loads on the  $y = 0.02357m$  wall at  $x = 0.114m$  for steady and transient inflow.

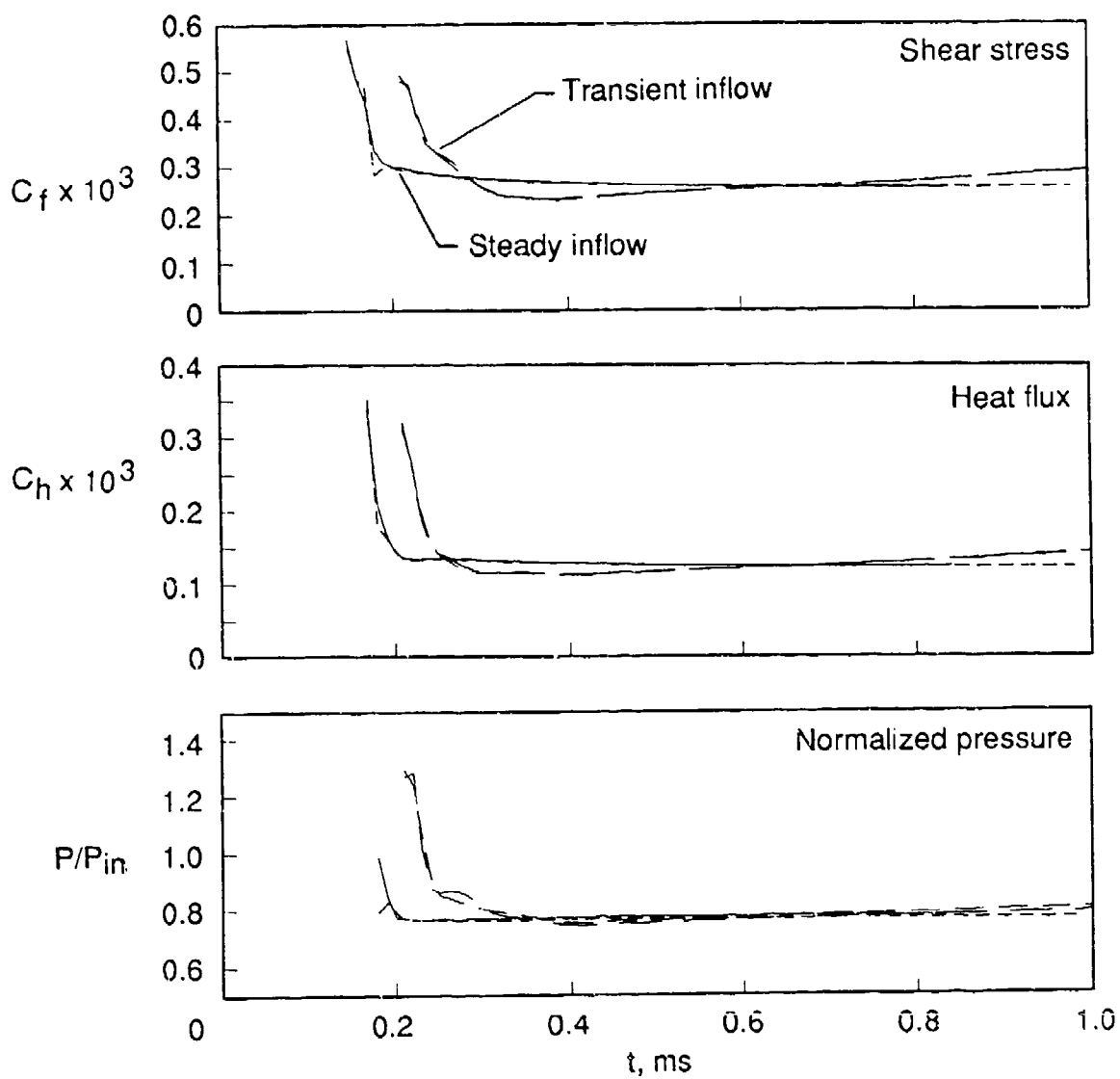


Figure 19: Comparison of loads on the  $y = 0.02357m$  wall at  $x = 0.5m$  for steady and transient inflow.

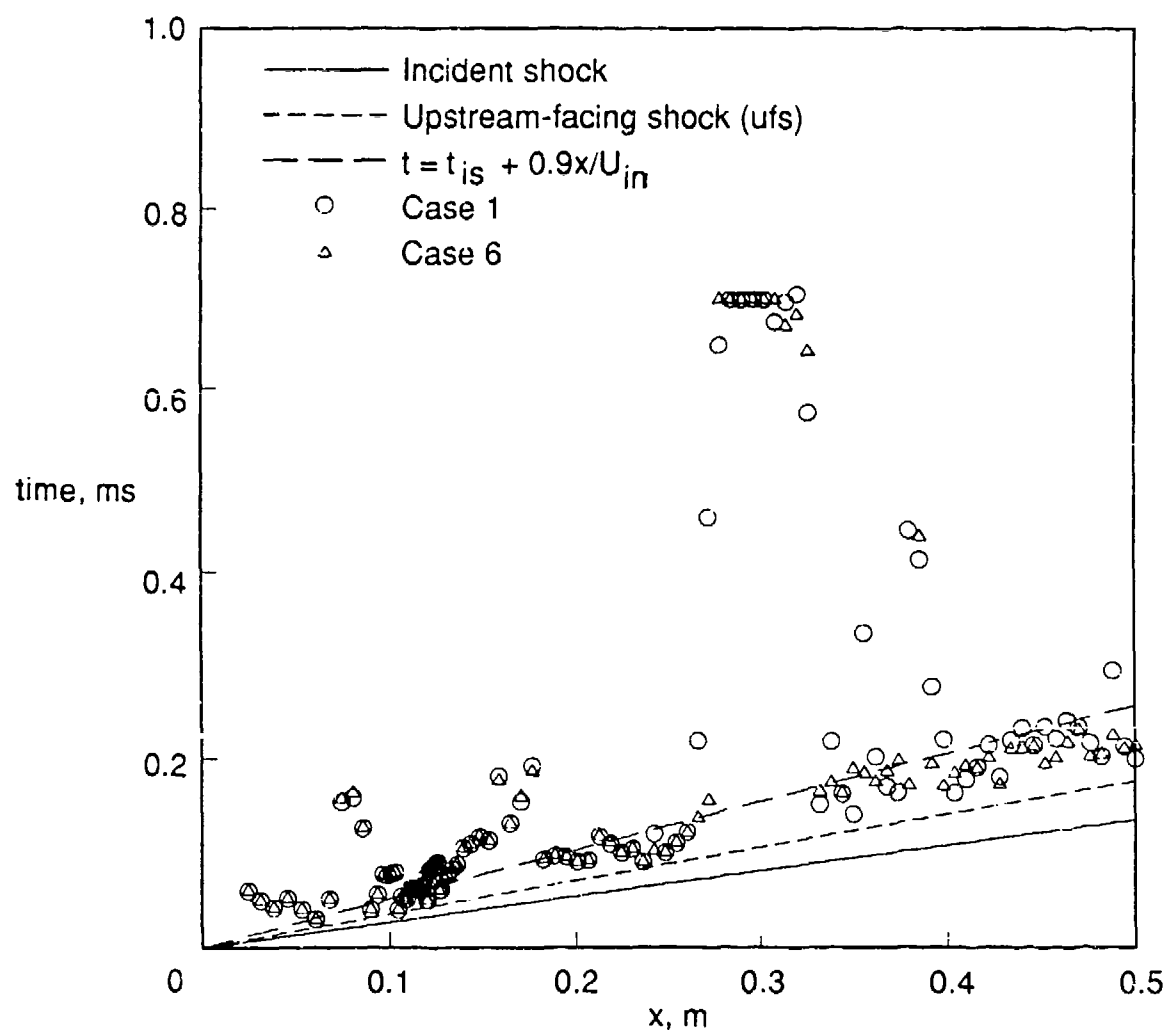


Figure 20: Establishment time for normalized pressure along the  $y = 0.02357m$  wall.

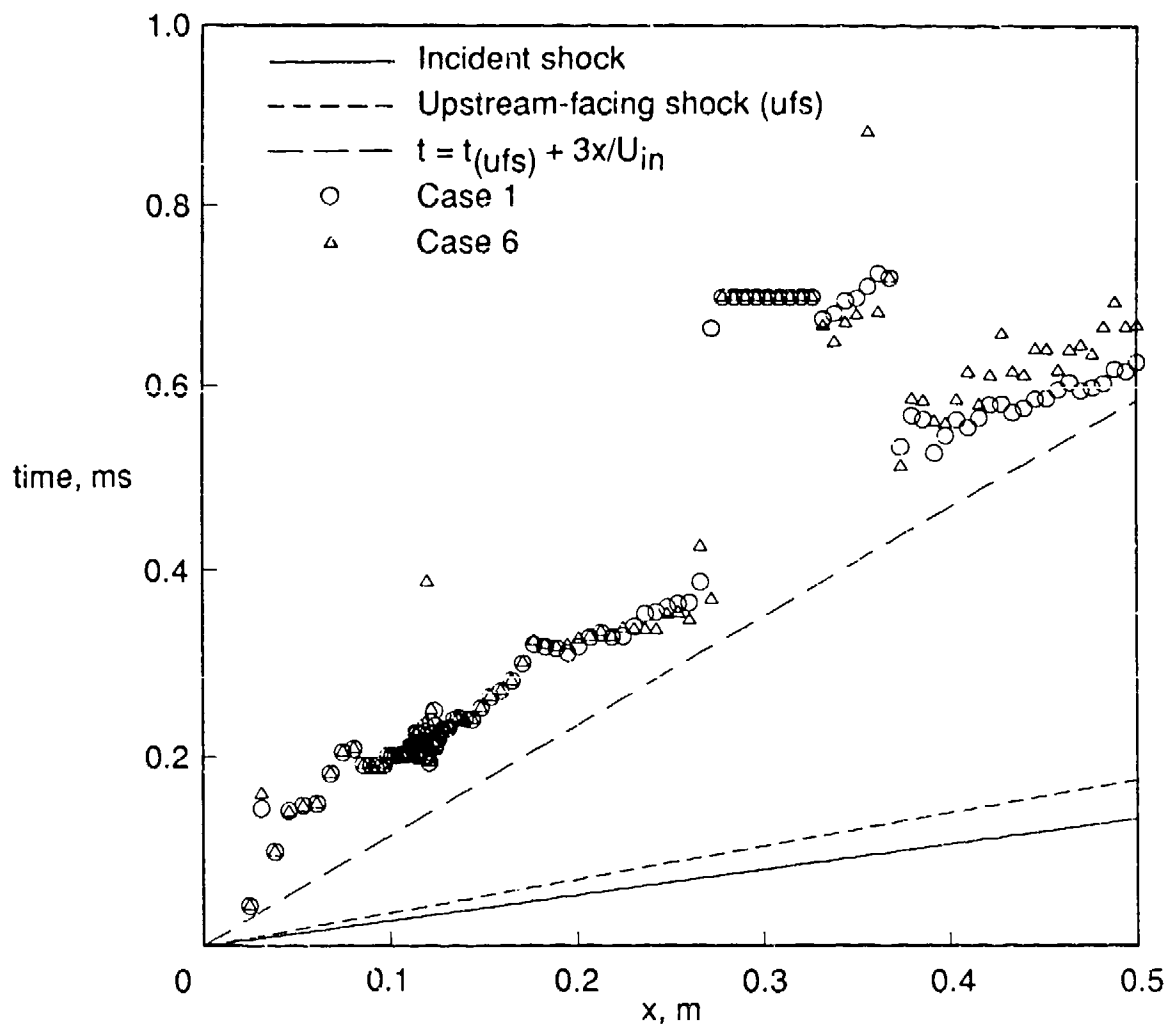


Figure 21: Establishment time for Stanton number along the  $y = 0.02357m$  wall.

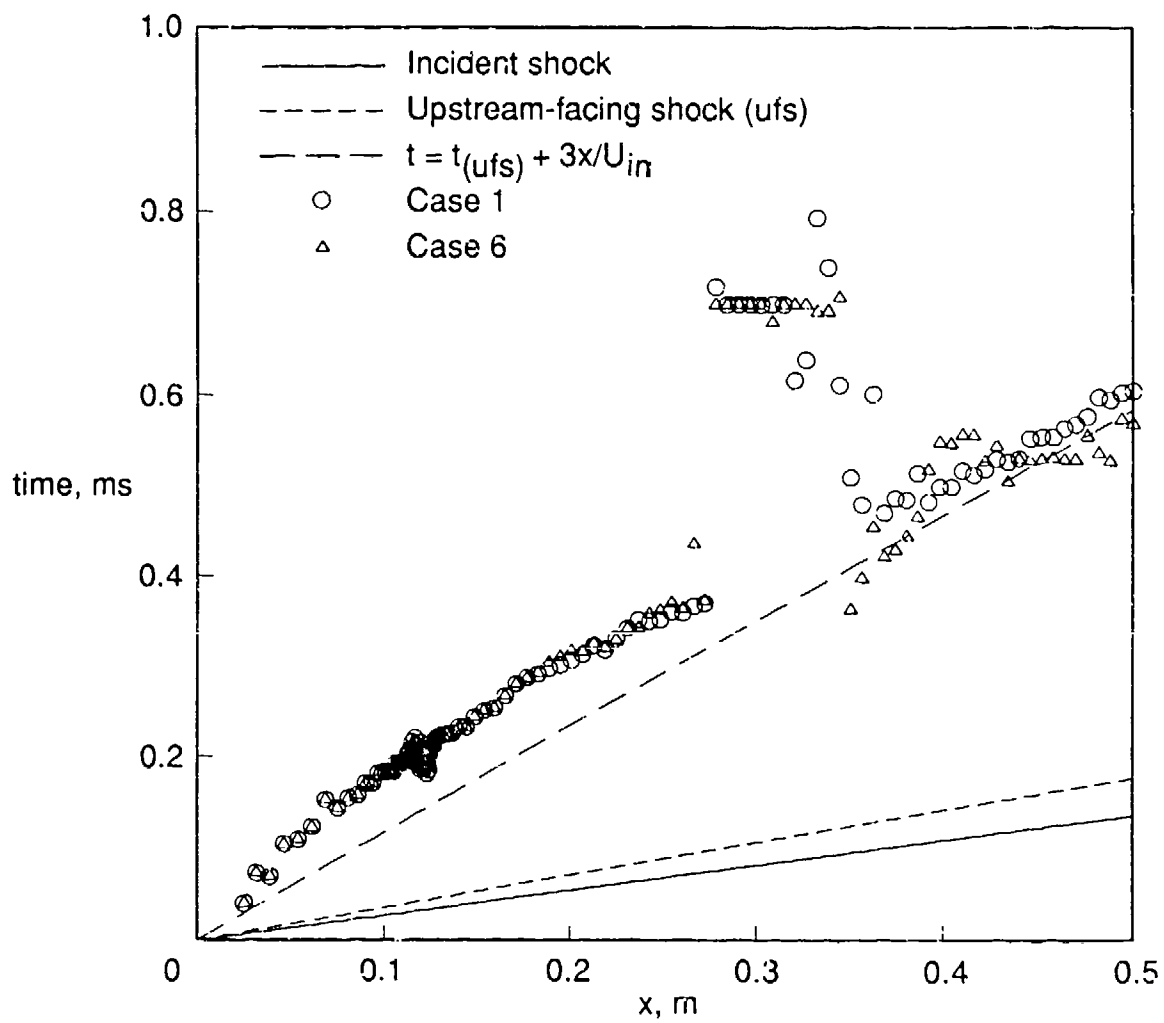


Figure 22: Establishment time for shear stress coefficient along the  $y = 0.02357m$  wall.